

# Topological Order and Non-Hermitian Skin Effect in Generalized Ideal Chern Bands

Jiong-Hao Wang<sup>✉,\*</sup>, Christopher Ekman<sup>✉</sup>, Raul Perea-Causin<sup>✉</sup>, Hui Liu<sup>✉</sup>, and Emil J. Bergholtz<sup>✉†</sup>  
*Department of Physics, Stockholm University, SE-106 91 Stockholm, Sweden*

(Dated: December 15, 2025)

Fractionalization in ideal Chern bands and non-Hermitian topological physics are two active but so far separate research directions. Merging these, we generalize the notion of ideal Chern bands to the non-Hermitian realm and uncover several striking consequences both on the level of band theory and in the strongly interacting regime. Specifically, we show that the lowest band of a Kapit–Mueller lattice model with an imaginary gauge potential satisfies a generalized ideal condition with complex Berry curvature in sync with a complex quantum metric. The ideal band remains purely real and exactly flat yet all right and left eigenstates accumulate at the boundaries on a cylinder, implying a non-Hermitian skin effect without an accompanying spectral winding. The skin effect is inherited by the many-body zero modes, yielding skin-Laughlin states with an exponential profile on the lattice. Moreover, at a critical strength of non-Hermiticity there is an unconventional phase transition on the torus, which is absent on the cylinder. Our findings lead to an extension of topological order in non-Hermitian systems.

Topological order is an organizing principle for quantum phases of strongly correlated systems with intrinsic long-range entanglement that lie beyond the conventional Landau paradigm of symmetry breaking [1]. A famous example is the fractional quantum Hall effect [2] and its zero-field analogue, fractional Chern insulators (FCIs) [3–19], which exhibit quantized Hall conductance and support quasiparticles obeying fractional anyonic statistics. Theoretical studies indicate that FCIs usually require topologically nontrivial flat bands with nearly ideal quantum geometry [20, 21], a condition recently realized experimentally in moiré materials, where zero-field FCIs have been observed at relatively high temperatures [22–28]. These advances bring FCIs closer to practical applications in quantum devices, and may enable fault-tolerant quantum computing [29]. However, in realistic settings, unavoidable couplings to the environment, such as to leads or measurement apparatus, introduce gain and dissipation, making the system effectively non-Hermitian [30], which can significantly affect the stability and properties of topological orders. Specifically, dissipation is naturally present in platforms hosting FCIs of bosons in the form of cold atoms [31–33], photons [34–37] and excitons [38, 39].

In parallel, non-Hermitian topology itself has recently emerged as a central topic of condensed matter, ranging from single-particle phenomena [30, 40–48] to many body effects [49–57], in which a variety of topological phases without Hermitian counterparts have been discovered [40–43, 53, 55, 58, 59]. Among these a striking manifestation is the so-called non-Hermitian skin effect (NHSE), where all eigenstates localize at system boundaries [45, 51, 60–65], often linked to the topology of spectra under open boundary conditions (OBCs) and periodic boundary conditions (PBCs) [66, 67], which has been observed in both classical systems [68–71] and open quantum systems [72, 73].

While numerous studies have treated topological order and non-Hermitian physics separately, the cross-fertilization between non-Hermitian physics and topological order remains essentially unexplored. Although non-Hermitian approaches

to FCIs have been theoretically explored in terms of dissipative preparation [31, 74] and particle loss [34, 52, 75], these works arrive at Hermitian FCI states lacking the NHSE. This motivates us to study the genuinely non-Hermitian FCIs with NHSE and their stability.

In this work, we investigate the Kapit–Mueller (KM) model [9] with an imaginary gauge potential. At the single-particle level, we find that the flat band surprisingly remains exactly real and flat despite the non-Hermiticity, while exhibits a NHSE, in contrast to the conventional situation where spectral topology is required. As the strength of the imaginary gauge potential  $\kappa$  increases, the gap between the flat band and excited bands decreases, yet the exact realness and flatness are preserved even as it moves across the excited states in the complex energy plane. Furthermore, the flat band still exhibits a complex generalization of ideal quantum geometry.

Including interactions at half filling, the non-Hermitian bosonic many-body system inherits NHSEs, leading to skin-Laughlin states on the cylinder. Albeit Laughlin-like states remain exact zero modes for all  $\kappa$ , above a critical  $\kappa_c$  they are no longer the ground states, as many other states acquire negative energy. Notably, the critical  $\kappa$  is much smaller than the single-particle gap-closing point even under the single-band projection [76], indicating the phase transition is intrinsic to the non-Hermitian ideal Chern band. For larger interaction strength, the critical  $\kappa$  gets larger, which serves as a manifestation of the breakdown of the variational principle in non-Hermitian systems.

*Non-Hermitian Kapit–Mueller model.*— We start from the following tight-binding Hamiltonian with an imaginary gauge potential  $\mathbf{A} = (i\kappa(\pi/2)(1 - \phi), 0, 0)$ ,

$$H_0(\kappa) = \sum_{i \neq j} e^{-\kappa(\pi/2)(1-\phi)(x_j - x_i)} J_{ij} a_i^\dagger a_j, \quad (1)$$

where  $a_i^\dagger$  ( $a_i$ ) creates (annihilates) a particle at site  $(x_i, y_i)$ . Here,  $J_{ij} = W_{ij} e^{-i\pi y_{ij}(x_i + x_j)\phi}$  denotes the hopping strength with  $W_{ij} = (-1)^{x_{ij} + y_{ij} + x_{ij} y_{ij}} e^{-(\pi/2)(1-\phi)(x_{ij}^2 + y_{ij}^2)}$ ,  $x_{ij} =$

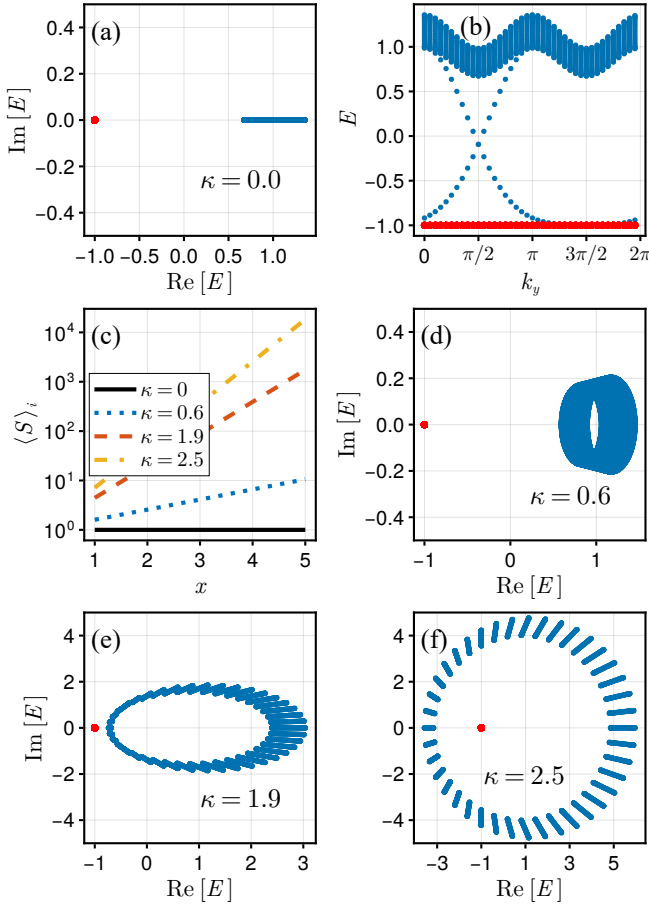


FIG. 1. **Non-Hermitian exact flat band.** (a) Energy spectrum of the Hermitian KM model on a torus. (b) Energy spectrum on the cylinder with OBCs in  $x$ , the same for Hermitian and non-Hermitian cases by virtue of the similarity transformation. Edge states emerge within the gap. (c) Skin-localization on the cylinder indicated by the expectation value  $\langle S \rangle_i$  of the similarity transformation operator  $S$  in terms of the single-particle state on lattice site  $i$  as a function of the  $x$  coordinate of site  $i$ . (d-f) Complex energy spectrum of the non-Hermitian KM model on the torus at  $\kappa = 0.6, 1.9$  and  $2.5$ , respectively. For (a) and (d-f), the red dot represents the flat band with degeneracy equal to the number of magnetic fluxes. We take flux  $\phi = 1/2$ .

$x_i - x_j$ , and  $y_{ij} = y_i - y_j$ . When  $\kappa = 0$ , the system reduces to the original Hermitian KM model [9] with rational magnetic flux  $\phi$  through each plaquette in the Landau gauge, leading to an exactly flat band [see Fig. 1(a)] with Landau level wave functions discretized on the lattice. With  $\kappa \neq 0$ , the Hamiltonian is non-Hermitian due to the non-reciprocal hopping between two sites.

In the cylinder geometry with OBCs along  $x$ , the Hamiltonian  $H_0(0)$  and  $H_0(\kappa)$  are related by a similarity transformation, i.e.,  $H_0(\kappa) = SH_0(0)S^{-1}$  with  $S = e^{\kappa(\pi/2)(1-\phi)\sum_i x_i a_i^\dagger a_i}$  [see the Supplemental Material (SM) [77] for an explicit proof]. Consequently, the energy spectrum at  $\kappa \neq 0$  remains identical to that of the Hermitian case, as shown in Fig. 1(b), where edge states appear within

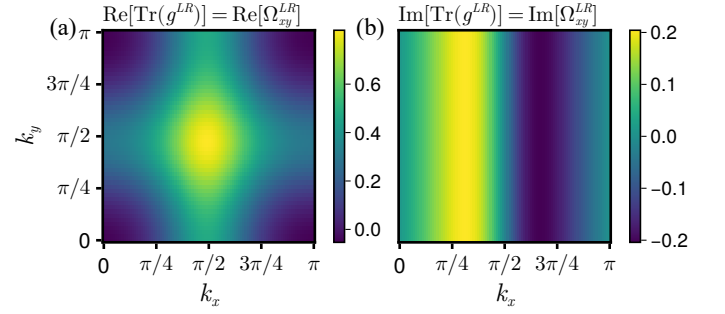


FIG. 2. **Generalized ideal quantum geometry.** (a) Real and (b) imaginary part of  $\text{Tr}(g^{LR})$  and  $\Omega_{xy}^{LR}$  which are exactly equal. We only show half of the magnetic Brillouin zone due to the translational invariance and take  $\phi = 1/2, \kappa = 0.6$ .

the gap between the flat band and excited bands. The associated left and right eigenstates are skewed to the two ends along the  $x$  direction, leading to the NHSE for all states. To verify this, Fig. 1(c) shows the expectation value  $\langle S \rangle_i = \langle i|S|i \rangle$ , with  $|i \rangle = a_i^\dagger |0 \rangle$  and  $|0 \rangle$  being the vacuum state. The linear behavior of  $\langle S \rangle_i$  as a function of  $x$  in the logarithmic scale directly visualizes how this imaginary gauge potential induces the exponential skin localization. With PBCs along  $x$ , the non-Hermitian and Hermitian Hamiltonians cannot be related by such a similarity transformation since the position operator is ill-defined. One might therefore expect the bands to acquire dispersions and imaginary parts, given that NHSE under OBCs is often related to a nontrivial spectral winding in the complex energy plane under PBCs [66, 67]. As we show below, however, this does *not* occur here.

**Generalized ideal Chern band.**— We now numerically calculate the energy spectrum of Hamiltonian (1) with  $\phi = 1/2$  at finite  $\kappa$  under torus geometry, i.e., PBCs along both directions. As shown in Fig. 1(d-f), surprisingly, the flat band, colored red, remains exactly flat and purely real, corresponding to an isolated point in the complex energy plane under the non-Hermitian deformation, with degeneracy fixed by the total flux through the system. This then demonstrates that the flat band of the non-Hermitian KM model provides a prominent example of NHSE without spectral winding, contrary to the usual expectation [66, 67]. As  $\kappa$  increases further, the loop formed by excited states expands, while the flat band remains pinned at  $E = -1$ . Consequently, the gap between the flat and excited bands closes and reopens at  $\kappa \sim 2$ .

In the Hermitian KM model, the flat band mimics the lowest Landau level in the continuum, and therefore has ideal quantum geometry satisfying the trace condition  $\text{Tr}[g] = |\Omega_{xy}|$  [20, 21] where  $g$  is the quantum metric and  $\Omega_{xy}$  is the Berry curvature. To study the quantum geometry of the non-Hermitian system [78–81] at finite  $\kappa$ , we calculate the non-Hermitian quantum geometric tensor

$$G_{\mu\nu}^{LR} = \langle \partial_{k_\mu} u_{\mathbf{k}}^L | (1 - |u_{\mathbf{k}}^R\rangle\langle u_{\mathbf{k}}^L|) | \partial_{k_\nu} u_{\mathbf{k}}^R \rangle, \quad (2)$$

where  $\mu, \nu = x, y$  and  $|u_{\mathbf{k}}^R\rangle, |u_{\mathbf{k}}^L\rangle$  are right and left eigenvectors with lattice momentum  $\mathbf{k} = (k_x, k_y)$  in the flat band.

The non-Hermitian quantum metric  $g_{\mu\nu}^{LR}$  and Berry curvature  $\Omega_{\mu\nu}^{LR}$  are defined as

$$g_{\mu\nu}^{LR} = (G_{\mu\nu}^{LR} + G_{\nu\mu}^{LR})/2, \quad (3)$$

$$\Omega_{\mu\nu}^{LR} = i(G_{\mu\nu}^{LR} - G_{\nu\mu}^{LR}). \quad (4)$$

It is straightforward to see that  $g_{\mu\nu}^{LR}$  is symmetric and that  $\Omega_{\mu\nu}^{LR}$  is antisymmetric, just as in the Hermitian case. Furthermore, the definitions of  $G_{\mu\nu}^{LR}$ ,  $g_{\mu\nu}^{LR}$  and  $\Omega_{\mu\nu}^{LR}$  reduce to their Hermitian counterparts for a Hermitian Hamiltonian due to the coincidence of left and right eigenvectors. In the Hermitian case, both  $g$  and  $\Omega_{xy}$  are real, while in the non-Hermitian case, both  $g_{\mu\nu}^{LR}$  and  $\Omega_{\mu\nu}^{LR}$  can be complex.

We calculate  $g_{\mu\nu}^{LR}$  and  $\Omega_{xy}^{LR}$  at  $\phi = 1/2$  and  $\kappa = 0.6$  as shown in Fig. 2. Due to the gauge choice in Hamiltonian (1), for  $\phi = 1/q$  with  $q$  being an integer, the magnetic unit cell contains  $q$  consecutive sites in the  $x$  direction, so the magnetic Brillouin zone is  $k_x \in [0, 2\pi/q)$  and  $k_y \in [0, 2\pi)$ . Here we show only half of the magnetic Brillouin zone as the quantum geometry has translational symmetry by  $\pi/q$  along  $k_y$  [82]. Although  $g_{\mu\nu}^{LR}$  and  $\Omega_{xy}^{LR}$  have nonzero imaginary parts [see Fig. 2(b)], we find that both the real and imaginary parts satisfy the *generalized ideal trace conditions*

$$\text{Re}[\text{Tr}(g)] = \pm \text{Re}[\Omega_{xy}], \quad (5)$$

$$\text{Im}[\text{Tr}(g)] = \pm \text{Im}[\Omega_{xy}], \quad (6)$$

which take plus signs in our case and also hold for the flat band of Eq. 1 at any rational  $\phi$ . The integral of  $\Omega_{xy}^{LR}$  over the magnetic Brillouin zone divided by  $2\pi$  gives Chern number  $C = 1$ . We therefore call the flat band a *generalized ideal Chern band*.

*Non-Hermitian topological order.*— Having confirmed the ideal condition of the non-Hermitian flat band, we next explore the existence of FCIs, by diagonalizing the bosonic Hamiltonian with onsite repulsive interactions,

$$H(\kappa) = H_0(\kappa) + \sum_j \frac{U}{2} a_j^\dagger a_j^\dagger a_j a_j. \quad (7)$$

With  $\kappa = 0$ , the Hermitian KM model at half filling gives rise to bosonic Laughlin states [9]. For a square lattice with  $L_x$  ( $L_y$ ) sites in  $x$  ( $y$ ) direction, the degeneracy of the flat band is  $N = L_x L_y / q$  for  $\phi = 1/q$  and the corresponding particle number at half-filling is  $n_b = N/2$ . We only consider commensurate cases that  $q, N, n_b$  are all integers. Because  $H(\kappa) = SH(0)S^{-1}$  [see SM [77]] on a cylinder with OBCs along  $x$ , the energy spectrum at nonzero  $\kappa$  is the same as the Hermitian case, but the eigenstates accumulate at the boundaries, leading to Laughlin states with NHSE as shown by the density  $\rho_b(i) = \langle \Psi^X | a_i^\dagger a_i | \Psi^{X'} \rangle$  in Fig. 3(a). Here  $|\Psi^X\rangle$  with  $X = R, L$  represents the right/left eigenvector of the Laughlin state. The biorthogonal density with  $X = L, X' = R$  is indicated by the black solid line, and the density of left and right eigenvectors with  $X = X' = L$  and  $X = X' = R$  is indicated by the red dashed and blue dotted line, respectively. Note that the biorthogonal density at any  $\kappa$  is identical

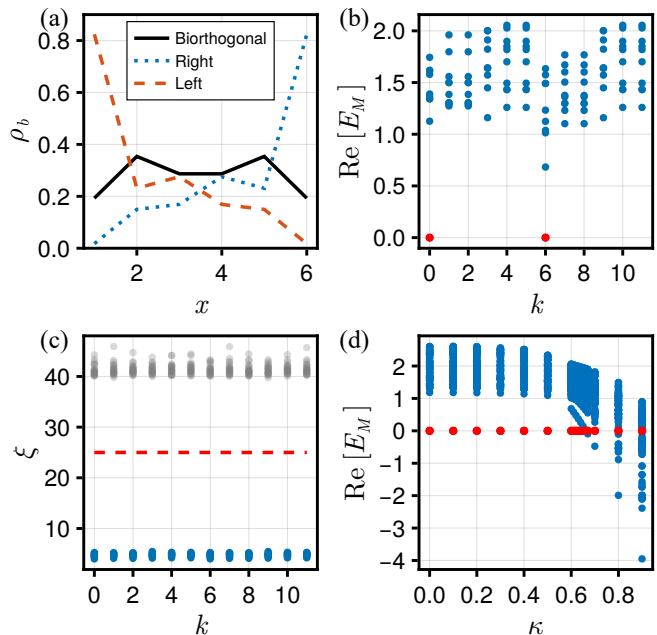


FIG. 3. **Skin-Laughlin states.** (a) Particle number density  $\rho_b$  of the ground state on the cylinder at  $\kappa = 1.9, U = 0.1$  as a function of the  $x$  coordinate for  $L_x = 6, L_y = 3$  corresponding to total particle number  $n_b = 5$  at  $\phi = 1/2$ , because of the integer shift  $N = 2n_b - 1$  for Laughlin states on the cylinder [83]. The biorthogonal density, identical to the Hermitian case is represented by the black solid line, and the density of right and left eigenstates is represented by the blue dotted and red dashed line, respectively, showing the skin effect of the non-Hermitian Laughlin states. (b) Real part of the many-body energy spectrum on the torus at  $\kappa = 0.6$  with the Laughlin states in red. (c) Particle entanglement spectrum of the Laughlin states in (b) for  $n_A = 3$ . The number of states below the gap is 112, consistent with the generalized Pauli principle. Note that  $\xi$  above the gap should be infinite in principle, and the finite value here is due to machine precision. (d) Real part of the energy spectrum with respect to  $\kappa$  with the Laughlin states in red, exhibiting the phase transition. All results in (b)-(d) are obtained with system size  $L_x = 6, L_y = 4$  at  $\phi = 1/2$  for the band projected interaction, under which the interaction strength is the only energy scale, chosen for arbitrary here.

to density of the Hermitian system [see SM [77]]. Because  $\rho_b$  is uniform in  $y$  direction, we only plot the variation of  $\rho_b$  with  $x$  coordinate. The accumulation of the density of left and right eigenvectors at the boundaries visualizes the skin-Laughlin states.

On the torus, we calculate the many-body energy spectrum numerically by projecting the interaction onto the flat band with the assumption that the interaction strength is much smaller than the single-particle energy gap [76] [see SM [77] for the process of projection validated by numerics in the non-Hermitian framework]. In Fig. 3(b), we show the real part of the energy at  $\phi = 1/2, \kappa = 0.6$  for  $L_x = 6, L_y = 4$  with respect to the momentum index  $k = k_1 + k_2 N_1$ , where  $k_1 = 0, 1, \dots, N_1 - 1$  and  $k_2 = 0, 1, \dots, N_2 - 1$  with  $N_1 = L_x/q, N_2 = L_y$  in our specific gauge choice. We observe two states at exactly zero energy [colored red in Fig. 3(b)] in the

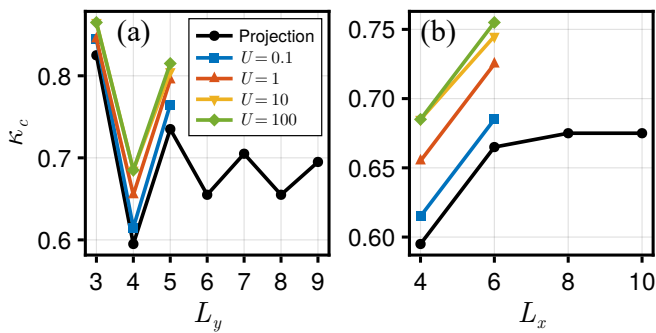


FIG. 4. **Many-body transition point.** Critical  $\kappa$  of the many-body phase transition at  $\phi = 1/2$  with and without the single-band projection for various interaction strength for (a)  $L_x = 4$ , with respect to  $L_y$  and (b)  $L_y = 4$ , with respect to  $L_x$ .

momentum sector predicted by the generalized Pauli principle for bosonic Laughlin states [3], with a finite gap to the excited states in the spectral flow [see SM [77]].

To further rule out possible competing orders, we calculate the particle entanglement spectrum [3]. We partition the total  $n_b$  bosons into  $A$  and  $B$  parts with  $n_A$  and  $n_B$  particles, respectively, and trace out the  $B$  part, arriving at a reduced density matrix  $\rho_A = \text{Tr}_B(\sum_i |\Psi_i^X\rangle\langle\Psi_i^{X'}|/2)$  where the summation is over all ground states. The eigenvalues of  $\rho_A$  are  $e^{-\xi}$  where  $\xi$  is the particle entanglement spectrum, as shown in Fig. 3(c), where we take  $X = X' = R$ . We see a significant gap in the particle entanglement spectrum indicated by the red dashed line, and the number of states below the gap is consistent with the generalized Pauli principle [3], confirming the ground states are FCIs [see more data on particle entanglement spectrum in SM [77]].

The robustness of the non-Hermitian Laughlin states against  $\kappa$  is shown in Fig. 3(d). Here, the energy gap decreases with  $\kappa$  and closes at  $\kappa_c \sim 0.7$ , which differs from the gap closing point of the single-particle spectrum at  $\kappa_0 \sim 2.0$ . Surprisingly, certain states drop to negative energy after the gap closing point, in stark contrast to the Hermitian case where the energy is positive semi-definite for repulsive interactions. As  $\kappa$  increases further, more and more states fall below zero energy, indicating a transition into a gapless regime as verified by the spectral flow [see SM [77]]. Remarkably, there is always a pair of real-energy states pinned at zero energy even in the gapless regime, as indicated by red color in Fig. 3(d), which are shown to be FCI states by the entanglement spectrum [see SM [77]]. We also find the energies of the few states with the lowest real parts are always purely real and the states show signatures of superfluid order [see SM [77]]. We remark that we view  $H(\kappa)$  as an effective non-Hermitian Hamiltonian, as would arise from an energy-independent retarded self-energy. In that sense, the real parts of the eigenvalues define the many-body resonance energies (ground vs excited sector), while the imaginary parts encode the corresponding lifetimes/broadenings.

We note that the presence of a finite  $\kappa_c$  is not a finite-size ef-

fect. To show this, we calculate  $\kappa_c$  for different system sizes. Our extrapolations converge for  $\phi = 1/2$  to  $\kappa_c \sim 0.7$ , well below the single-particle scale  $\kappa_0 \sim 2.0$ . Due to computational restraints, we keep one of  $L_x, L_y$  fixed and increase the other. As shown by the black line in Fig. 4(a), at  $L_x = 4$ ,  $\kappa_c$  oscillates as  $L_y$  increases for odd and even  $L_y$  while the oscillating amplitude decays, showing a tendency to converge to a value about 0.7. For  $L_y = 4$ , as shown in Fig. 4(b),  $\kappa_c$  increases monotonically as  $L_x$  only takes even values under our choice of magnetic unit cells and converges to  $\kappa_c \sim 0.7$ , close to that in Fig. 4(b), implying  $\kappa_c$  remains finite and smaller than  $\kappa_0$  in the thermodynamic limit.

Further including the remote band shows the persistence of such a many-body phase transition. Here, we evaluate the many-body energy spectrum without band projection as a function of interaction strength  $U$ , as shown in Fig. 4. All the way up to the hard-core limit [see SM [77]], the transition point  $\kappa$  is always smaller than  $\kappa_0$ . Based on intuition from the variational principle in Hermitian systems, one may expect that  $\kappa_c$  will not increase if we discard the single-band approximation and raise  $U$ . That is because for large  $U$ , the single-band approximation is invalid and the Hamiltonian is diagonalized within a larger Hilbert space. According to the variational principle, the enlarged Hilbert space leads to lower ground state energy and thus a smaller  $\kappa_c$  is expected to enter a gapless regime with negative energy. However, we surprisingly find that  $\kappa_c$  gets larger as  $U$  increases [see Fig. 4], in stark contrast to the insight from Hermitian quantum mechanics, which can be attributed to the breakdown of the conventional variational principle in non-Hermitian systems.

*Discussion.*— We have investigated the interplay between topological order, the non-Hermitian skin effect, and generalized ideal quantum geometry at both the single-particle and many-body level. The non-interacting model hosts a purely real and exactly flat band which satisfies a generalized ideal condition for quantum geometry and furthermore exhibits the NHSE, thus contradicting the common conception that the NHSE is accompanied by spectral winding.

The physics of the interacting model depends on the underlying manifold. On a cylinder, the ground state is a skin-Laughlin state for all values of the non-Hermiticity  $\kappa$ . On a torus, in contrast, we found that Laughlin states are the ground states only for  $\kappa$  below a critical value, while for larger  $\kappa$ , negative energy states outcompete the zero modes. This was found by projecting to the generalized ideal Chern band, and the phase transition on the torus can therefore be attributed to intrinsic properties of the generalized ideal Chern band rather than to influence from the other bands. Going beyond the single-band projection, we found that the critical value of  $\kappa$  increases with the interaction strength, demonstrating the breakdown of the variational principle familiar from Hermitian quantum mechanics.

A useful way to view our results is as a kind of competition between non-Hermitian skin effects and topological order, with a silver lining for subcritical  $\kappa$  in that the lack of spectral winding allows for the survival of topological or-

der. Despite the strong spectral sensitivity usually associated with the NHSE, for  $\kappa < \kappa_c$  our numerics, along with general arguments for Laughlin-type topological order, indicate that the twofold ground-state manifold on the torus still realizes topological order in Wen's sense [1]. The biorthogonal ground-state projector  $P_{\text{GS}} = \sum_{a=1}^2 |\Psi_a^R\rangle\langle\Psi_a^L|$  is adiabatically connected to that of the Hermitian Kapit–Mueller FCI, so the ground-state degeneracy, anyon structure and entanglement properties are expected to remain unchanged, and generic local perturbations that preserve the many-body gap should split the torus doublet only by amplitudes that are exponentially small in the system size. In this subcritical regime non-Hermitian skin effects and topological order therefore genuinely coexist: the NHSE reshapes the right/left wave functions into “skin-Laughlin” states without destroying their topological content. For  $\kappa > \kappa_c$  on the torus, however, the spectral rearrangement induced by the NHSE promotes more extended states to the bottom of the spectrum; the Laughlin manifold, while still present as biorthogonal eigenstates with the same topological signatures, moves out of the ground-state sector so that skin effect and topological order effectively compete.

Our work opens a new direction in the study of non-Hermitian topological order and indicates several intriguing avenues for future research. First, the properties of our generalized ideal Chern bands suggest the existence of rigorous index theorems for many-body zero modes that apply more generally. Second, the negative energy states on the torus require more detailed investigation by advanced numerical tools. Third, it would be interesting to explore whether the NHSE leads to novel responses of the FCI states. Fourth, it would be interesting to connect our findings to recent work on mixed-state topological order [84–86] where non-unitary dynamics and coupling to environments are built-in from the outset. Fifth, an alternative description of dynamical effects in dissipative FCIs within the framework of quantum master equations is challenging but intriguing [74, 75].

Finally, while the main motivation of our work is conceptual we note that it may apply, *mutatis mutandis*, to systems ranging from AMO platforms such as rotating BECs [33], cold atoms [32, 87] and photonics [34–37] where dissipation is ubiquitous, to solid state moiré heterostructures where bosonic FCIs are predicted to form in nearly ideal Chern bands of excitons with long but finite and tunable lifetimes [38, 39].

*Acknowledgments*—We thank helpful discussions with Kang Yang, Daniel Varjas and Fan Yang. This work was supported by the Swedish Research Council (2024-04567), the Knut and Alice Wallenberg Foundation (2023.0256), and the Göran Gustafsson Foundation for Research in Natural Sciences and Medicine.

† emil.bergholtz@fysik.su.se

- [1] X.-G. Wen, Colloquium: Zoo of quantum-topological phases of matter, *Rev. Mod. Phys.* **89**, 041004 (2017).
- [2] H. L. Stormer, Nobel lecture: The fractional quantum hall effect, *Rev. Mod. Phys.* **71**, 875 (1999).
- [3] N. Regnault and B. A. Bernevig, Fractional Chern insulator, *Phys. Rev. X* **1**, 021014 (2011).
- [4] Z. Liu and E. J. Bergholtz, Recent developments in fractional Chern insulators, in *Encyclopedia of Condensed Matter Physics (Second Edition)*, edited by T. Chakraborty (Academic Press, Oxford, 2024) second edition ed., pp. 515–538.
- [5] E. J. Bergholtz and Z. Liu, Topological flat band models and fractional Chern insulators, *International Journal of Modern Physics B* **27**, 1330017 (2013).
- [6] S. A. Parameswaran, R. Roy, and S. L. Sondhi, Fractional quantum Hall physics in topological flat bands, *Comptes Rendus Physique* **14**, 816 (2013), topological insulators / Isolants topologiques.
- [7] A. Kol and N. Read, Fractional quantum Hall effect in a periodic potential, *Phys. Rev. B* **48**, 8890 (1993).
- [8] G. Möller and N. R. Cooper, Composite fermion theory for bosonic quantum Hall states on lattices, *Phys. Rev. Lett.* **103**, 105303 (2009).
- [9] E. Kapit and E. Mueller, Exact parent Hamiltonian for the quantum Hall states in a lattice, *Phys. Rev. Lett.* **105**, 215303 (2010).
- [10] E. Tang, J.-W. Mei, and X.-G. Wen, High-Temperature fractional quantum Hall states, *Phys. Rev. Lett.* **106**, 236802 (2011).
- [11] K. Sun, Z. Gu, H. Katsura, and S. Das Sarma, Nearly flatbands with nontrivial topology, *Phys. Rev. Lett.* **106**, 236803 (2011).
- [12] T. Neupert, L. Santos, C. Chamon, and C. Mudry, Fractional quantum Hall states at zero magnetic field, *Phys. Rev. Lett.* **106**, 236804 (2011).
- [13] D. Sheng, Z.-C. Gu, K. Sun, and L. Sheng, Fractional quantum Hall effect in the absence of Landau levels, *Nature Communications* **2**, 1 (2011).
- [14] A. Abouelkomsan, Z. Liu, and E. J. Bergholtz, Particle-hole duality, emergent Fermi liquids, and fractional Chern insulators in moiré flatbands, *Phys. Rev. Lett.* **124**, 106803 (2020).
- [15] C. Repellin and T. Senthil, Chern bands of twisted bilayer graphene: Fractional Chern insulators and spin phase transition, *Phys. Rev. Res.* **2**, 023238 (2020).
- [16] P. J. Ledwith, G. Tarnopolsky, E. Khalaf, and A. Vishwanath, Fractional Chern insulator states in twisted bilayer graphene: An analytical approach, *Phys. Rev. Research* **2**, 023237 (2020).
- [17] Z. Liu, A. Abouelkomsan, and E. J. Bergholtz, Gate-tunable fractional Chern insulators in twisted double bilayer graphene, *Phys. Rev. Lett.* **126**, 026801 (2021).
- [18] H. Li, U. Kumar, K. Sun, and S.-Z. Lin, Spontaneous fractional Chern insulators in transition metal dichalcogenide moiré superlattices, *Phys. Rev. Res.* **3**, L032070 (2021).
- [19] P. Wilhelm, T. C. Lang, and A. M. Läuchli, Interplay of fractional Chern insulator and charge density wave phases in twisted bilayer graphene, *Phys. Rev. B* **103**, 125406 (2021).
- [20] P. J. Ledwith, A. Vishwanath, and E. Khalaf, Family of ideal Chern flatbands with arbitrary Chern number in chiral twisted graphene multilayers, *Phys. Rev. Lett.* **128**, 176404 (2022).
- [21] J. Wang and Z. Liu, Hierarchy of ideal flatbands in chiral twisted multilayer graphene models, *Phys. Rev. Lett.* **128**, 176403 (2022).
- [22] Y. Xie, A. T. Pierce, J. M. Park, D. E. Parker, E. Khalaf, P. Ledwith, Y. Cao, S. H. Lee, S. Chen, P. R. Forrester, K. Watanabe, T. Taniguchi, A. Vishwanath, P. Jarillo-Herrero, and A. Yacoby, Fractional Chern insulators in magic-angle twisted bilayer graphene, *Nature* **600**, 439 (2021).

---

\* jionghao.wang@fysik.su.se

- [23] H. Park, J. Cai, E. Anderson, Y. Zhang, J. Zhu, X. Liu, C. Wang, W. Holtzmann, C. Hu, Z. Liu, T. Taniguchi, K. Watanabe, J.-H. Chu, T. Cao, L. Fu, W. Yao, C.-Z. Chang, D. Cobden, D. Xiao, and X. Xu, Observation of fractionally quantized anomalous Hall effect, *Nature* **622**, 74 (2023).
- [24] J. Cai, E. Anderson, C. Wang, X. Zhang, X. Liu, W. Holtzmann, Y. Zhang, F. Fan, T. Taniguchi, K. Watanabe, Y. Ran, T. Cao, L. Fu, D. Xiao, W. Yao, and X. Xu, Signatures of fractional quantum anomalous Hall states in twisted MoTe<sub>2</sub>, *Nature* **622**, 63 (2023).
- [25] Y. Zeng, Z. Xia, K. Kang, J. Zhu, P. Knüppel, C. Vaswani, K. Watanabe, T. Taniguchi, K. F. Mak, and J. Shan, Thermodynamic evidence of fractional Chern insulator in moiré MoTe<sub>2</sub>, *Nature* **622**, 69 (2023).
- [26] F. Xu, Z. Sun, T. Jia, C. Liu, C. Xu, C. Li, Y. Gu, K. Watanabe, T. Taniguchi, B. Tong, J. Jia, Z. Shi, S. Jiang, Y. Zhang, X. Liu, and T. Li, Observation of integer and fractional quantum anomalous Hall effects in twisted bilayer MoTe<sub>2</sub>, *Phys. Rev. X* **13**, 031037 (2023).
- [27] Z. Lu, T. Han, Y. Yao, A. P. Reddy, J. Yang, J. Seo, K. Watanabe, T. Taniguchi, L. Fu, and L. Ju, Fractional quantum anomalous Hall effect in multilayer graphene, *Nature* **626**, 759 (2024).
- [28] H. Park, W. Li, C. Hu, C. Beach, M. Gonçalves, J. F. Mendez-Valderrama, J. Herzog-Arbeitman, T. Taniguchi, K. Watanabe, D. Cobden, L. Fu, B. A. Bernevig, N. Regnault, J.-H. Chu, D. Xiao, and X. Xu, Observation of high-temperature dissipationless fractional chern insulator (2025), arXiv:2503.10989 [cond-mat].
- [29] C. Nayak, S. H. Simon, A. Stern, M. Freedman, and S. Das Sarma, Non-abelian anyons and topological quantum computation, *Rev. Mod. Phys.* **80**, 1083 (2008).
- [30] Y. Ashida, Z. Gong, and M. Ueda, Non-hermitian physics, *Adv. Phys.* **69**, 249 (2020).
- [31] M. Roncaglia, M. Rizzi, and J. I. Cirac, Pfaffian state generation by strong three-body dissipation, *Phys. Rev. Lett.* **104**, 096803 (2010).
- [32] J. Léonard, S. Kim, J. Kwan, P. Segura, F. Grusdt, C. Repellin, N. Goldman, and M. Greiner, Realization of a fractional quantum hall state with ultracold atoms, *Nature* **619**, 495 (2023).
- [33] N. Cooper, Rapidly rotating atomic gases, *Advances in Physics* **57**, 539 (2008), <https://doi.org/10.1080/00018730802564122>.
- [34] M. Hafezi, M. D. Lukin, and J. M. Taylor, Non-equilibrium fractional quantum hall state of light, *New J. Phys.* **15**, 063001 (2013).
- [35] E. Kapit, M. Hafezi, and S. H. Simon, Induced self-stabilization in fractional quantum hall states of light, *Phys. Rev. X* **4**, 031039 (2014).
- [36] L. W. Clark, N. Schine, C. Baum, N. Jia, and J. Simon, Observation of Laughlin states made of light, *Nature* **582**, 41 (2020).
- [37] P. D. Kurilovich, V. D. Kurilovich, J. Lebreuilly, and S. M. Girvin, Stabilizing the Laughlin state of light: Dynamics of hole fractionalization, *SciPost Phys.* **13**, 107 (2022).
- [38] M. Xie, M. Hafezi, and S. Das Sarma, Long-lived topological flatband excitons in semiconductor moiré heterostructures: A bosonic Kane-Mele model platform, *Phys. Rev. Lett.* **133**, 136403 (2024).
- [39] R. Perea-Causin, H. Liu, and E. J. Bergholtz, Exciton fractional Chern insulators in moiré heterostructures, *Phys. Rev. Res.* **7**, L042033 (2025).
- [40] E. J. Bergholtz, J. C. Budich, and F. K. Kunst, Exceptional topology of non-hermitian systems, *Rev. Mod. Phys.* **93**, 015005 (2021).
- [41] Z. Gong, Y. Ashida, K. Kawabata, K. Takasan, S. Higashikawa, and M. Ueda, Topological phases of non-hermitian systems, *Phys. Rev. X* **8**, 031079 (2018).
- [42] K. Kawabata, K. Shiozaki, M. Ueda, and M. Sato, Symmetry and topology in non-hermitian physics, *Phys. Rev. X* **9**, 041015 (2019).
- [43] F. Song, S. Yao, and Z. Wang, Non-hermitian topological invariants in real space, *Phys. Rev. Lett.* **123**, 246801 (2019).
- [44] K. Yokomizo and S. Murakami, Non-bloch band theory for non-hermitian systems, *Phys. Rev. Lett.* **123**, 066404 (2019).
- [45] Y. Ma and T. L. Hughes, Quantum skin hall effect, *Phys. Rev. B* **108**, L100301 (2023).
- [46] Z. Li and R. S. K. Mong, Homotopical characterization of non-Hermitian band structures, *Phys. Rev. B* **103**, 155129 (2021).
- [47] C. C. Wojcik, X.-Q. Sun, T. Bzduszek, and S. Fan, Homotopy characterization of non-hermitian hamiltonians, *Phys. Rev. B* **101**, 205417 (2020).
- [48] K. Yang, Z. Li, J. L. K. König, L. Rødland, M. Stålhammar, and E. J. Bergholtz, Homotopy, Symmetry, and non-Hermitian Band Topology, *Rep. Prog. Phys.* **87**, 078002 (2024).
- [49] R. Hamazaki, K. Kawabata, and M. Ueda, Non-hermitian many-body localization, *Phys. Rev. Lett.* **123**, 090603 (2019).
- [50] C. H. Lee, Many-body topological and skin states without open boundaries, *Phys. Rev. B* **104**, 195102 (2021).
- [51] F. Alsallom, L. Herviou, O. V. Yazyev, and M. Brzezińska, Fate of the non-hermitian skin effect in many-body fermionic systems, *Phys. Rev. Res.* **4**, 033122 (2022).
- [52] T. Yoshida, K. Kudo, and Y. Hatsugai, Non-hermitian fractional quantum hall states, *Sci. Rep.* **9**, 16895 (2019).
- [53] E. Lee, H. Lee, and B.-J. Yang, Many-body approach to non-hermitian physics in fermionic systems, *Phys. Rev. B* **101**, 121109 (2020).
- [54] K. Yang, S. C. Morampudi, and E. J. Bergholtz, Exceptional spin liquids from couplings to the environment, *Phys. Rev. Lett.* **126**, 077201 (2021).
- [55] K. Kawabata, K. Shiozaki, and S. Ryu, Many-body topology of non-hermitian systems, *Phys. Rev. B* **105**, 165137 (2022).
- [56] D.-W. Zhang, Skin superfluid, topological mott insulators, and asymmetric dynamics in an interacting non-hermitian Aubry-André-Harper model, *Phys. Rev. B* **101**, 10.1103/PhysRevB.101.235150 (2020).
- [57] V. Meden, L. Grunwald, and D. M. Kennes,  $\mathcal{PT}$ -symmetric, non-hermitian quantum many-body physics—a methodological perspective, *Rep. Prog. Phys.* **86**, 124501 (2023).
- [58] K. Ding, C. Fang, and G. Ma, Non-hermitian topology and exceptional-point geometries, *Nat. Rev. Phys.* **4**, 745 (2022).
- [59] N. Okuma and M. Sato, Non-hermitian topological phenomena: A review, *Annu. Rev. Condens. Matter Phys.* **14**, 83 (2023).
- [60] T. E. Lee, Anomalous edge state in a non-hermitian lattice, *Phys. Rev. Lett.* **116**, 133903 (2016).
- [61] Y. Xiong, Why does bulk boundary correspondence fail in some non-hermitian topological models, *J. Phys. Comm.* **2**, 035043 (2018).
- [62] S. Yao and Z. Wang, Edge states and topological invariants of non-hermitian systems, *Phys. Rev. Lett.* **121**, 086803 (2018).
- [63] F. K. Kunst, E. Edvardsson, J. C. Budich, and E. J. Bergholtz, Biorthogonal bulk–boundary correspondence in non-hermitian systems, *Phys. Rev. Lett.* **121**, 026808 (2018).
- [64] V. M. Martínez Álvarez, J. E. Barrios Vargas, and L. E. F. Foa Torres, Non-hermitian robust edge states in one dimension: Anomalous localization and eigenspace condensation at exceptional points, *Phys. Rev. B* **97**, 121401 (2018).
- [65] J. Gliozzi, G. De Tomasi, and T. L. Hughes, Many-body non-hermitian skin effect for multipoles, *Phys. Rev. Lett.* **133**, 136503 (2024).
- [66] N. Okuma, K. Kawabata, K. Shiozaki, and M. Sato, Topolog-

- ical origin of non-hermitian skin effect, *Phys. Rev. Lett.* **124**, 086801 (2020).
- [67] K. Zhang, Z. Yang, and C. Fang, Correspondence between winding numbers and skin modes in non-hermitian systems, *Phys. Rev. Lett.* **125**, 126402 (2020).
- [68] M. Brandenbourger, X. Locsin, E. Lerner, and J. van Wezel, Non-reciprocal robotic metamaterials, *Nat. Commun.* **10**, 4608 (2019).
- [69] L. Xiao, T. Deng, K. Wang, G. Zhu, Z. Wang, W. Yi, and P. Xue, Non-hermitian bulk–boundary correspondence in quantum dynamics, *Nat. Phys.* **16**, 761 (2020).
- [70] T. Helbig, T. Hofmann, S. Imhof, M. Abdelghany, T. Kiessling, L. W. Molenkamp, C. H. Lee, A. Szameit, M. Greiter, and R. Thomale, Generalized bulk–boundary correspondence in non-hermitian topoelectrical circuits, *Nat. Phys.* **16**, 747 (2020).
- [71] S. Weidemann, M. Kremer, S. Longhi, and A. Szameit, Topological funneling of light, *Science* **368**, 311 (2020).
- [72] Q. Liang, D. Xie, Z. Dong, H. Li, H. Li, B. Gadway, W. Yi, and B. Yan, Dynamic signatures of non-hermitian skin effect and topology in ultracold atoms, *Phys. Rev. Lett.* **129**, 070401 (2022).
- [73] E. Zhao, Z. Wang, C. He, T. F. J. Poon, K. K. Pak, Y.-J. Liu, P. Ren, X.-J. Liu, and G.-B. Jo, Two-dimensional non-hermitian skin effect in an ultracold fermi gas, *Nature* **637**, 565 (2025).
- [74] Z. Liu, E. J. Bergholtz, and J. C. Budich, Dissipative preparation of fractional chern insulators, *Phys. Rev. Research* **3**, 043119 (2021).
- [75] T. Yoshida, K. Kudo, H. Katsura, and Y. Hatsugai, Fate of fractional quantum hall states in open quantum systems: Characterization of correlated topological states for the full liouvillian, *Phys. Rev. Research* **2**, 033428 (2020).
- [76] D. Yoshioka, B. I. Halperin, and P. A. Lee, Ground state of two-dimensional electrons in strong magnetic fields and 1/3 quantized hall effect, *Phys. Rev. Lett.* **50**, 1219 (1983).
- [77] In the Supplemental Material, we prove the similarity transformation for relating Hermitian and non-Hermitian Hamiltonian on a cylinder, show additional details on the single-band projection procedure in the non-Hermitian context and numerical proof, provide more numerical data on spectral flow, entanglement spectrum, signatures of superfluid, many-body energy spectrum beyond the single-band projection and results for  $\phi = 1/3$ .
- [78] J. Behrends, R. Ilan, and M. Goldstein, Quantum geometry of non-hermitian systems (2025), arXiv:2503.13604 [quant-ph].
- [79] C. Chen Ye, W. L. Vleeshouwers, S. Heatley, V. Gritsev, and C. Morais Smith, Quantum metric of non-hermitian suschrieffer-heeger systems, *Phys. Rev. Res.* **6**, 023202 (2024).
- [80] Y.-M. R. Hu, E. A. Ostrovskaya, and E. Estrecho, Generalized quantum geometric tensor in a non-hermitian exciton-polariton system [invited], *Opt. Mater. Exp.* **14**, 664 (2024).
- [81] K. Yang, Z. Li, P. Xue, E. J. Bergholtz, and P. W. Brouwer, Spontaneous chern-euler duality transitions (2025), arXiv:2503.21861 [cond-mat].
- [82] D. Varjas, A. Abouelkomsan, K. Yang, and E. Bergholtz, Topological lattice models with constant berry curvature, *Scipost Phys.* **12**, 118 (2022).
- [83] Z. Liu, D. L. Kovrizhin, and E. J. Bergholtz, Bulk-edge correspondence in fractional chern insulators, *Phys. Rev. B* **88**, 081106 (2013).
- [84] R. Fan, Y. Bao, E. Altman, and A. Vishwanath, Diagnostics of mixed-state topological order and breakdown of quantum memory, *PRX Quantum* **5**, 020343 (2024).
- [85] Z. Wang, Z. Wu, and Z. Wang, Intrinsic mixed-state topological order, *PRX Quantum* **6**, 010314 (2025).
- [86] T. D. Ellison and M. Cheng, Toward a classification of mixed-state topological orders in two dimensions, *PRX Quantum* **6**, 010315 (2025).
- [87] N. R. Cooper, J. Dalibard, and I. B. Spielman, Topological bands for ultracold atoms, *Rev. Mod. Phys.* **91**, 015005 (2019).
- [88] M. E. Fisher, M. N. Barber, and D. Jasnow, Helicity modulus, superfluidity, and scaling in isotropic systems, *Phys. Rev. A* **8**, 1111 (1973).
- [89] A. Paramekanti, N. Trivedi, and M. Randeria, Upper bounds on the superfluid stiffness of disordered systems, *Phys. Rev. B* **57**, 11639 (1998).

## SUPPLEMENTAL MATERIAL

In the Supplemental Material, we prove the similarity transformation for relating Hermitian and non-Hermitian Hamiltonian on a cylinder, show additional details on the single-band projection procedure in the non-Hermitian context and numerical proof, provide more numerical data on spectral flow, entanglement spectrum, signatures of superfluid, many-body energy spectrum beyond the single-band projection and results for  $\phi = 1/3$ .

## SIMILARITY TRANSFORMATION FOR NON-HERMITIAN SKIN EFFECT

In this section, we prove both the single-particle and many-body Hamiltonian under non-Hermitian deformation in the main text can be related to their Hermitian counterparts by a similarity transformation on a cylinder, from which the non-Hermitian skin effect is clear. We take the second quantization formulation in the proof.

The single-particle Hamiltonian of the Kapit-Mueller (KM) model in Eq.1 of the main text reads

$$H_0(\kappa) = \sum_{i \neq j} e^{-\gamma(x_j - x_i)} J_{ij} a_i^\dagger a_j, \quad (8)$$

where we denote  $\gamma = \kappa(\pi/2)(1 - \phi)$  for simplicity. The similarity transformation operator is  $S(\kappa) = e^{\gamma \sum_i x_i a_i^\dagger a_i} = e^{\gamma \sum_i x_i n_i}$  with  $n_j = a_j^\dagger a_j$  being the particle number operator. As the number operators commute with each other, we have  $S^{-1}(\kappa) =$

$e^{-\gamma \sum_i x_i n_i}$ . In the following, we prove the relation

$$H_0(\kappa) = S(\kappa)H_0(0)S^{-1}(\kappa) \quad (9)$$

independent of whether  $a_i^\dagger$  ( $a_i$ ) is the creation (annihilation) operator of bosons or fermions. The most important tool in the proof is the Baker-Campbell-Hausdorff (BCH) formula

$$e^A B e^{-A} = B + [A, B] + \frac{1}{2!}[A, [A, B]] + \dots + \frac{1}{n!}[A, [A, \dots [A, B]]] \quad (10)$$

where  $A, B$  are operators,  $[...]$  denotes the commutator and  $n$  is an integer tending to infinity. Using the BCH formula, we can directly obtain

$$S(\kappa)a_i^\dagger a_j S^{-1}(\kappa) = a_i^\dagger a_j + \gamma(x_i - x_j)a_i^\dagger a_j + \frac{1}{2!}[\gamma(x_i - x_j)]^2 a_i^\dagger a_j + \dots + \frac{1}{n!}[\gamma(x_i - x_j)]^n a_i^\dagger a_j \quad (11)$$

$$= e^{\gamma(x_i - x_j)} a_i^\dagger a_j, \quad (12)$$

where we have used the equation  $[\sum_m x_m a_m^\dagger a_m, a_i^\dagger a_j] = (x_i - x_j)a_i^\dagger a_j$ , which can be proved easily for both bosons and fermions. Therefore, the single-particle case Eq. 9 is proved.

The many-body Hamiltonian for interacting bosons in Eq. 7 in the main text is  $H(\kappa) = H_0(\kappa) + H_I$  with

$$H_I = \sum_j \frac{U}{2} a_j^\dagger a_j^\dagger a_j a_j = \sum_j \frac{U}{2} n_j (n_j - 1) \quad (13)$$

As number operators commute, it is obvious that  $H_I$  is invariant under the similarity transformation by  $S$  also from BCH formula. Combining Eq. 9, we arrive at  $H(\kappa) = S(\kappa)H(0)S^{-1}(\kappa)$  for the total Hamiltonian of interacting bosons. Therefore, the right and left eigenvectors  $|\Psi^R(\kappa)\rangle$  and  $|\Psi^L(\kappa)\rangle$  of  $H(\kappa)$  are related to the eigenstate  $|\Psi\rangle$  of the Hermitian Hamiltonian  $H(0)$  by

$$|\Psi^R(\kappa)\rangle = S(\kappa)|\Psi\rangle, \quad (14)$$

$$\langle \Psi^L(\kappa) | = \langle \Psi | S^{-1}(\kappa), \quad (15)$$

leading to the non-Hermitian skin effect.

By the similarity transformation, we can prove on the cylinder the biorthogonal number density defined in the main text

$$\rho_b(i) = \langle \Psi^L(\kappa) | a_i^\dagger a_i | \Psi^R(\kappa) \rangle \quad (16)$$

$$= \langle \Psi | S^{-1}(\kappa) a_i^\dagger a_i S(\kappa) | \Psi \rangle \quad (17)$$

$$= \langle \Psi | a_i^\dagger a_i | \Psi \rangle, \quad (18)$$

which is identical to the particle number density of the Hermitian state  $|\Psi\rangle$ . In the proof, we have used the commuting relation  $[S(\kappa), a_i^\dagger a_i] = 0$ .

## SINGLE-BAND PROJECTION IN THE NON-HERMITIAN CONTEXT

In this section, we provide details of the single-band projection in the non-Hermitian context and show the validity of this approximation numerically.

For generality, we consider a general free-particle Hamiltonian with translational invariance

$$H_f = \sum_{k, \alpha, \beta} a_{k, \alpha}^\dagger H_f^{\alpha, \beta}(k) a_{k, \beta}, \quad (19)$$

where  $k$  is the index of the lattice momentum,  $\alpha, \beta$  are internal degrees of freedom within a unit cell and  $H_f^{\alpha, \beta}(k)$  is the matrix element of the first-quantized Hamiltonian  $H_f(k)$ . For a non-Hermitian system,  $H_f(k)$  is a non-Hermitian matrix which can be diagonalized as

$$H_f(k) = \sum_{n, k} \epsilon_{n, k} |u_n^R(k)\rangle \langle u_n^L(k)|, \quad (20)$$



where  $\epsilon_{n,k}$  is the eigenenergy of band  $n$  and  $|u_n^R(k)\rangle$  and  $|u_n^L(k)\rangle$  are the corresponding right and left eigenvectors satisfying  $\langle u_n^L(k)|u_m^R(k)\rangle = \delta_{nm}$ . The second quantized Hamiltonian Eq. 19 can be written as

$$H_f = \sum_{n,k} \epsilon_{n,k} c_{n,k}^+ c_{n,k}, \quad (21)$$

where

$$c_{n,k}^+ = \sum_{\alpha} [u_n^R(k)]_{\alpha} a_{k,\alpha}^{\dagger}, \quad (22)$$

$$c_{n,k} = \sum_{\alpha} [u_n^L(k)]_{\alpha}^* a_{k,\alpha}, \quad (23)$$

with  $[u_n^R(k)]_{\alpha}$  ( $[u_n^L(k)]_{\alpha}$ ) being the amplitude of the wave function  $|u_n^R(k)\rangle$  ( $|u_n^L(k)\rangle$ ) on the internal orbital  $\alpha$ . Due to the biorthonormalization relation  $\langle u_n^L(k)|u_m^R(k)\rangle = \delta_{nm}$ ,  $c_{n,k}$  and  $c_{n,k}^+$  keep the original statistics of  $a_{k,\beta}$  and  $a_{k,\alpha}^{\dagger}$ , i.e., for bosons satisfying the commuting relations  $[c_{n_1,k_1}, c_{n_2,k_2}] = 0$ ,  $[c_{n_1,k_1}^+, c_{n_2,k_2}^+] = 0$ ,  $[c_{n_1,k_1}, c_{n_2,k_2}^+] = \delta_{n_1 n_2} \delta_{k_1 k_2}$  and for fermions satisfying the anti-commuting relations  $\{c_{n_1,k_1}, c_{n_2,k_2}\} = 0$ ,  $\{c_{n_1,k_1}^+, c_{n_2,k_2}^+\} = 0$ ,  $\{c_{n_1,k_1}, c_{n_2,k_2}^+\} = \delta_{n_1 n_2} \delta_{k_1 k_2}$ . However,  $c_{n,k}$  and  $c_{n,k}^+$  are not Hermitian conjugate of each other, thus we use  $+$  instead of  $\dagger$ . Therefore,  $c_{n,k}$  and  $c_{n,k}^+$  can be viewed as non-Hermitian generalization of creation and annihilation operators.

Eq. 22 and 23 represent a similarity transformation because of the biorthonormalization relation. Therefore we can get the inverse transformation

$$a_{k,\alpha}^{\dagger} = \sum_n [u_n^L(k)]_{\alpha}^* c_{n,k}^+, \quad (24)$$

$$a_{k,\alpha} = \sum_n [u_n^R(k)]_{\alpha} c_{n,k}. \quad (25)$$

Then for a general interaction in momentum space

$$V_I = \sum_{k_1, \alpha_1, k_2, \alpha_2, k_3, \alpha_3, k_4, \alpha_4} U(k_1, \alpha_1, k_2, \alpha_2, k_3, \alpha_3, k_4, \alpha_4) a_{k_1, \alpha_1}^{\dagger} a_{k_2, \alpha_2}^{\dagger} a_{k_3, \alpha_3} a_{k_4, \alpha_4} \quad (26)$$

$$= \sum_{k_1, n_1, k_2, n_2, k_3, n_3, k_4, n_4} \tilde{U}(k_1, n_1, k_2, n_2, k_3, n_3, k_4, n_4) c_{n_1, k_1}^+ c_{n_2, k_2}^+ c_{n_3, k_3} c_{n_4, k_4}, \quad (27)$$

where

$$\tilde{U}(k_1, n_1, k_2, n_2, k_3, n_3, k_4, n_4) = \sum_{\alpha_1, \alpha_2, \alpha_3, \alpha_4} U(k_1, \alpha_1, k_2, \alpha_2, k_3, \alpha_3, k_4, \alpha_4) [u_{n_1}^L(k_1)]_{\alpha_1}^* [u_{n_2}^L(k_2)]_{\alpha_2}^* [u_{n_3}^R(k_3)]_{\alpha_3} [u_{n_4}^R(k_4)]_{\alpha_4}. \quad (28)$$

Numerically, we can diagonalize  $V_I$  in the Fock basis associated with  $c_{n,k}$  and  $c_{n,k}^+$  like in the conventional Hermitian Fock basis (actually biorthogonal Fock basis here). If we focus on a single band indexed by  $n_0$  and assume the effect from other bands is negligible, we arrive at

$$V_I \approx \sum_{k_1, k_2, k_3, k_4} \tilde{U}(k_1, n_0, k_2, n_0, k_3, n_0, k_4, n_0) c_{n_0, k_1}^+ c_{n_0, k_2}^+ c_{n_0, k_3} c_{n_0, k_4}. \quad (29)$$

To validate the single-band projection for non-Hermitian systems, we calculate the many-body spectrum of Eq. 7 in the main text both with and without the projection, as shown in Fig. 5. Fig. 5(a) and (b) shows the real part of the energy spectrum at  $\kappa = 0.5$ , at which zero modes are ground states, and (a) is calculated under single-band projection and (b) without projection at interaction strength  $U = 0.001$ . We see the energy spectrum in (a) and (b) are the same. Note that for (b) the kinetic energy  $E_{kin} = n_b E_{flat}$  has been subtracted with  $n_b$  being the particle number and  $E_{flat} = -1$  the single-particle energy of the flat band, and the energy has been normalized to the same scale as (a) where the interaction strength is the only energy scale and chosen arbitrarily. Similarly, Fig. 5(c) and (d) are also the same for  $\kappa = 0.7$ , after the zero modes transition out of the ground state sector. Therefore, we show the validity of the single-band projection in the non-Hermitian context.

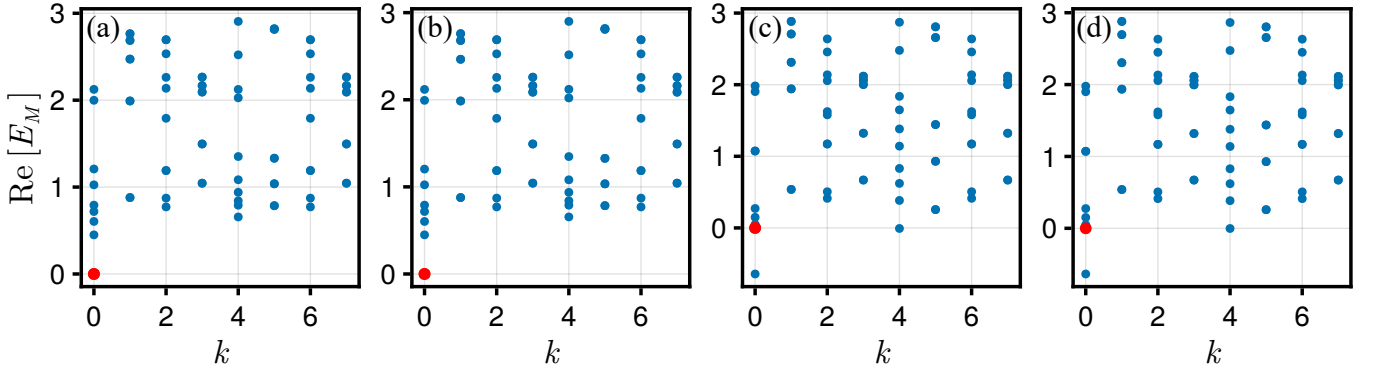


FIG. 5. Real part of the many-body energy spectrum with and without the single-band projection for system size  $L_x = 4$ ,  $L_y = 4$  and flux  $\phi = 1/2$ . (a) With single-band projection at  $\kappa = 0.5$ . (b) Without single-band projection at  $\kappa = 0.5$  and  $U = 0.001$ . (c) With single-band projection at  $\kappa = 0.7$ . (d) Without single-band projection at  $\kappa = 0.7$  and  $U = 0.001$ . For (b) and (d), the single-particle energy has been subtracted and the energy has been renormalized to the same scale as (a) and (c).

### SPECTRAL FLOW

In this section, we exhibit the spectral flow to show the existence of a finite gap in the regime with fractional Chern insulators (FCIs) as ground states, and the gapless nature of the system after FCIs transition out of the ground state sector.

In Fig. 6, We show the spectral flow under twisted boundary phase  $\Phi_x$  ( $\Phi_y$ ) along  $x$  ( $y$ ) direction. We show the spectral flow at  $\kappa = 0.6$  about  $\Phi_x$  and  $\Phi_y$  in Fig. 6(a) and (b), respectively, where we see a persistent finite gap between the FCIs (indicated by red color) and excited states. At  $\kappa = 0.67$ , close to the transition point, as shown in Fig. 6(c), we see the single state with negative energy under no twisted boundary phase can float above zero energy during the spectral flow and become indistinguishable from the dense excited states at some points, implying the system is gapless. When we further increase  $\kappa$  to 0.9, as shown in Fig. 6(d), more states drop below zero energy and we cannot identify an isolated manifold of states in the spectral flow pattern, further indicating the gapless nature of the system.

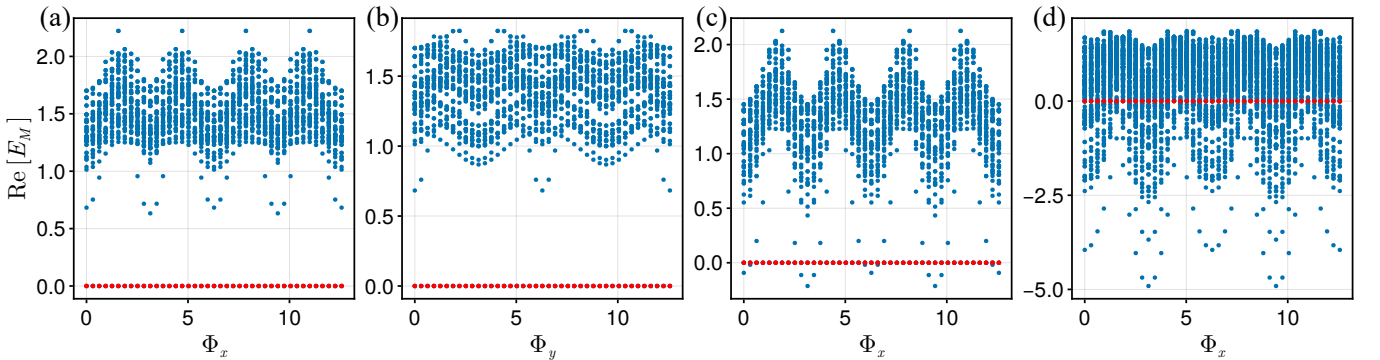


FIG. 6. (a)-(b) Spectral flow at  $\kappa = 0.6$  about (a)  $\Phi_x$  and (b)  $\Phi_y$ . (a)-(b) Spectral flow about  $\Phi_x$  at (c)  $\kappa = 0.67$  and (d)  $\kappa = 0.9$ . The system size is  $L_x = 6$ ,  $L_y = 4$  and flux is  $\phi = 1/2$ .

### ENTANGLEMENT SPECTRUM

In this section, we show more data on the entanglement spectrum to confirm the zero modes are FCIs.

We calculate the entanglement spectrum using the right eigenvectors of the zero modes, i.e.,  $X = X' = R$  for  $\rho_A = \text{Tr}_B(\sum_i |\Psi_i^X\rangle\langle\Psi_i^{X'}|/2)$ , for system size  $L_x = 6$ ,  $L_y = 4$  as shown in Fig. 7. We show results for the Hermitian case ( $\kappa = 0$ ) in the left column, the non-Hermitian FCI phase ( $\kappa = 0.6$ ) in the middle column and the phase with negative energy ( $\kappa = 0.8$ ) in the right column. In all the subfigures, we see a large gap indicated by the red dashed line. The number of states below the gap is 54 for the first row with  $n_A = 2$  and 112 for the second row with  $n_A = 3$ , consistent with the generalized Pauli principle.

Therefore, the entanglement spectrum verifies that the exact zero modes are FCIs, even in the presence of negative energy states. Note that  $\xi$  of the states above the gap is infinite in principle and arises at finite value in our plot due to the machine precision.

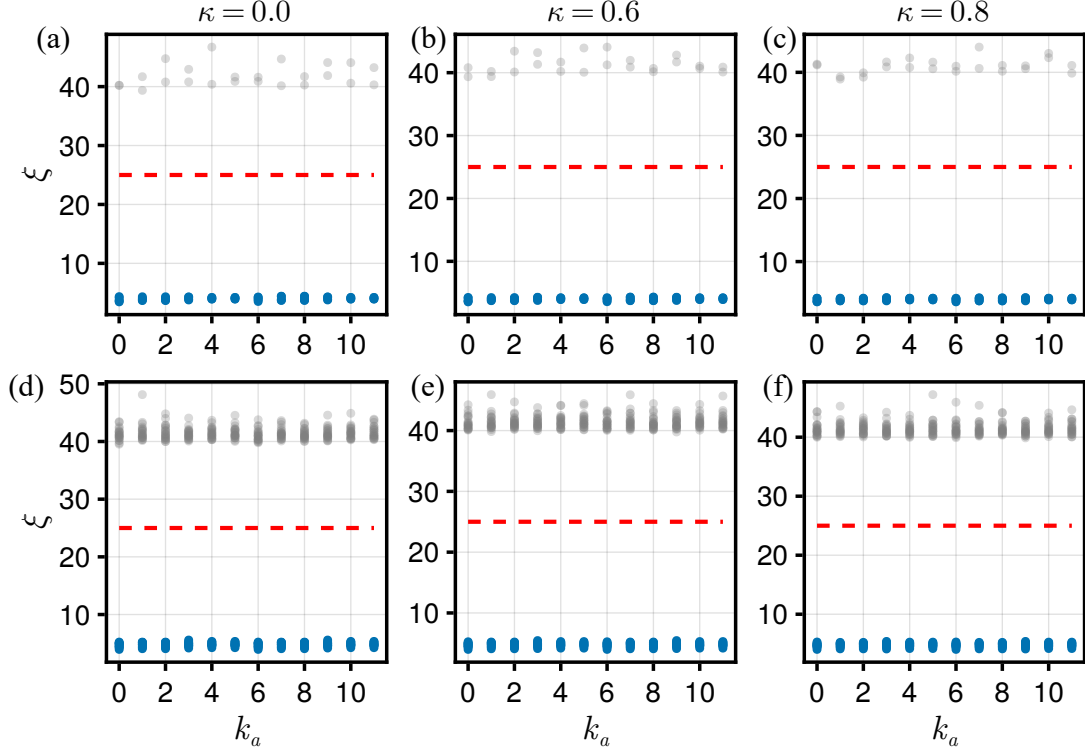


FIG. 7. Entanglement spectrum calculated using the right eigenvectors of the zero modes for  $L_x = 6, L_y = 4, \phi = 1/2$ .  $n_A = 2$  for (a)-(c) and  $n_A = 3$  for (d)-(f).

We also calculate the particle entanglement spectrum using left eigenvectors, i.e.,  $X = X' = L$ , and see the spectrum is almost the same as that of the right eigenvector. For the biorthogonal case with  $X = L, X' = R$ , the particle entanglement spectrum has imaginary parts, while the real part is still similar to Fig. 7 with a significant gap and number of states below the gap consistent with the counting rule.

### SIGNATURES OF SUPERFLUID

In this section, we show evidence of superfluid for the negative energy states competing with FCIs by calculating the superfluid density.

We calculate the superfluid density by the second derivative of the many-body state energy with respect to the twisted boundary phase  $\Phi_x$  ( $\Phi_y$ ) close to  $\Phi_x = 0$  ( $\Phi_y = 0$ ) [88, 89]

$$\rho_{s,y} = \frac{L_y}{L_x} \frac{\partial^2 E_M}{\partial \Phi_y^2} \Big|_{\Phi_y=0}, \quad (30)$$

$$\rho_{s,x} = \frac{L_x}{L_y} \frac{\partial^2 E_M}{\partial \Phi_x^2} \Big|_{\Phi_x=0}, \quad (31)$$

where  $\rho_{s,x}$  and  $\rho_{s,y}$  are superfluid density along  $x$  and  $y$  directions, respectively. We show  $\rho_{s,x}$  and  $\rho_{s,y}$  of the lowest energy state at  $\kappa = 0.7$  and  $0.75$  in Fig. 8, for which the energy is negative. We see as the system size  $L_x$  and  $L_y$  increase,  $\rho_{s,x}$  and  $\rho_{s,y}$  grow in overall, implying the negative energy states host nonzero superfluid density.

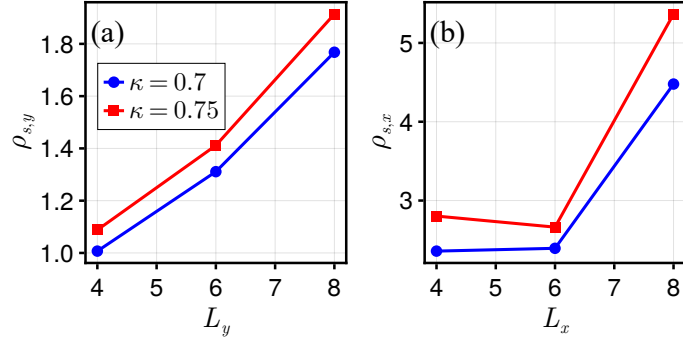


FIG. 8. Superfluid density (a)  $\rho_{s,y}$  as a function of  $L_y$  for  $L_x = 4$  and  $\rho_{s,x}$  as a function of  $L_x$  for  $L_y = 4$ .

### BEYOND THE SINGLE-BAND PROJECTION

In this section, we demonstrate the many-body energy spectrum under larger interaction strength without single-band projection.

We show the many-body energy spectrum without the single-band projection as a function of  $\kappa$  under  $U = 1, 10$  and  $100$  in Fig. 9(a),(b) and (c), respectively. For all the cases, we see FCIs as the ground states below a critical  $\kappa$  and transitions into a regime with negative energy states for larger  $\kappa$ .  $U = 100$  shows the physics in the hard-core limit, on the opposite side of the single-band projection. Therefore our finding is general for the whole range of interaction strength.

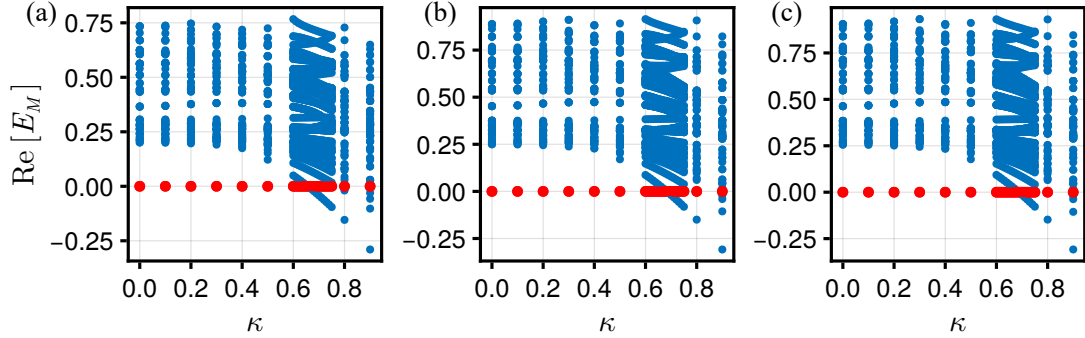


FIG. 9. Many-body energy spectrum without the single-band projection as a function of  $\kappa$  under (a)  $U = 1$ , (b)  $U = 10$  and (c)  $U = 100$  at  $L_x = 4, L_y = 4, \phi = 1/2$ .

To show  $U = 100$  is in the hard-core limit, we compare the many-body energy spectrum of  $U = 100$  and  $U = 1000$  as shown in Fig. 10. We cannot tell the difference between (a) with  $U = 100$  and (b) with  $U = 1000$  at  $\kappa = 0.6$  and similarly (c) and (d) at  $\kappa = 0.9$ , indicating  $U = 100$  is large enough to show the physics of hard-core bosons.

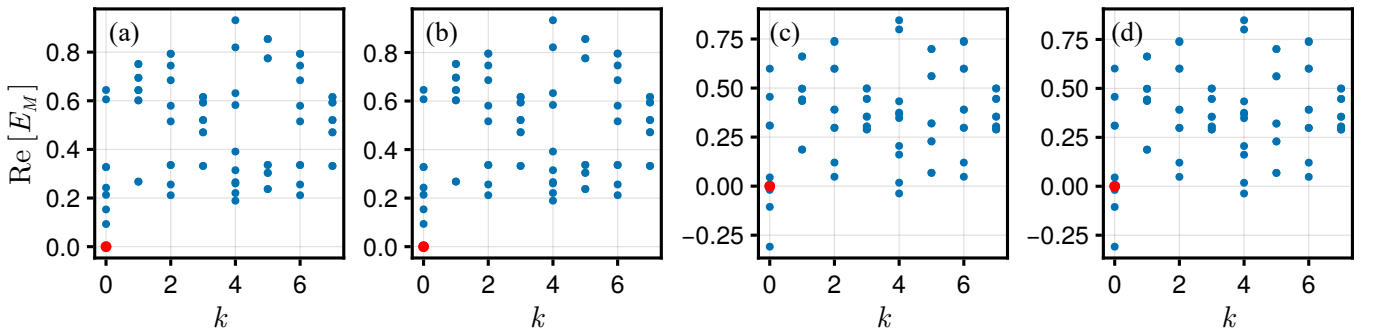


FIG. 10. Real part of the many-body energy spectrum at  $L_x = L_y = 4, \phi = 1/2$ . (a)  $U = 100, \kappa = 0.6$ , (b)  $U = 1000, \kappa = 0.6$ , (c)  $U = 100, \kappa = 0.9$ , (d)  $U = 1000, \kappa = 0.9$ .

$\phi = 1/3$  CASE

In this section, we show numerical results at flux  $\phi = 1/3$  to illuminate the generality of our findings.

In Fig. 11, we show the complex energy of the non-Hermitian KM model in Eq. 1 of the main text with  $\kappa = 0, 1, 1.4, 2$  from left to right. The same as the  $\phi = 1/2$  case, we see the flat band also remains exactly real and flat under the non-Hermitian deformation. The flat band energy is pinned at  $E = -1$  and the loop formed by excited states enlarges as  $\kappa$  increases. After the gap closing, the flat band tunnels into the loop while remain intact.

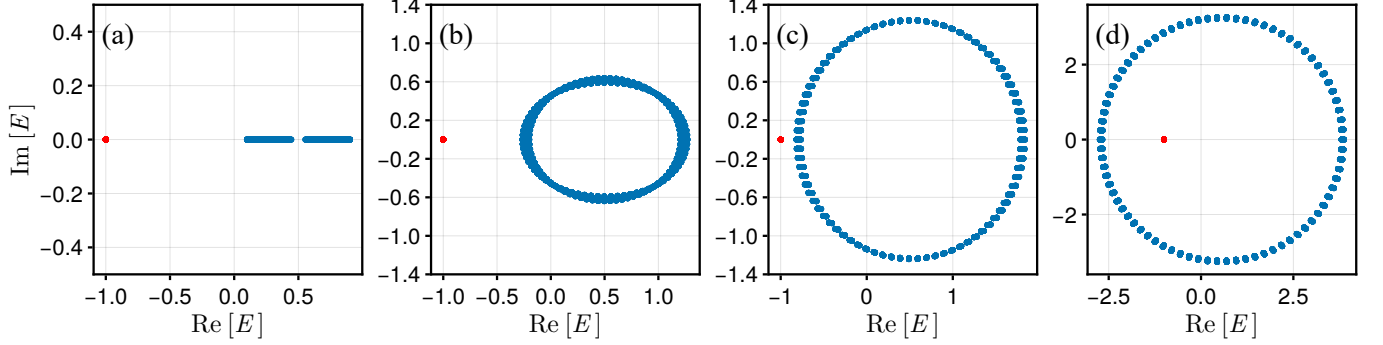


FIG. 11. Single-particle energy in the complex energy plane of the non-Hermitian KM model at  $\phi = 1/3$  for (a)  $\kappa = 0$  (b)  $\kappa = 1$  (c)  $\kappa = 1.4$  (d)  $\kappa = 2$ .

The real and imaginary parts of the quantum geometry at  $\phi = 1/3$  are shown in Fig. 12(a) and (b), respectively. The quantum geometry at  $\phi = 1/3$  also satisfies the generalized ideal condition in Eq. (5)(6) in the main text.

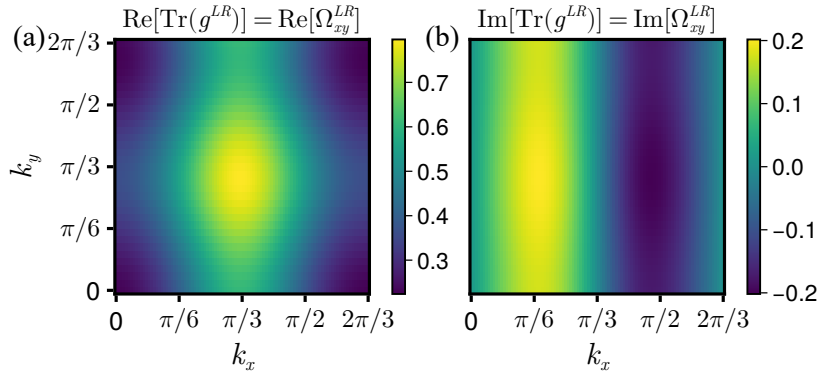


FIG. 12. (a) Real and (b) imaginary part of the quantum geometry at  $\phi = 1/3$  of one-third of the magnetic Brillouin zone.

In Fig. 13, we show the real part of the many-body energy spectrum at  $\kappa = 0.0, 0.7$  and  $0.8$  in (a), (b) and (c), respectively. We see zero-energy modes as the ground states at  $\kappa = 0.7$ , while at  $\kappa = 0.8$ , negative energy states emerge. The transition is shown in Fig. 13(c) by the energy spectrum as a function of  $\kappa$ .

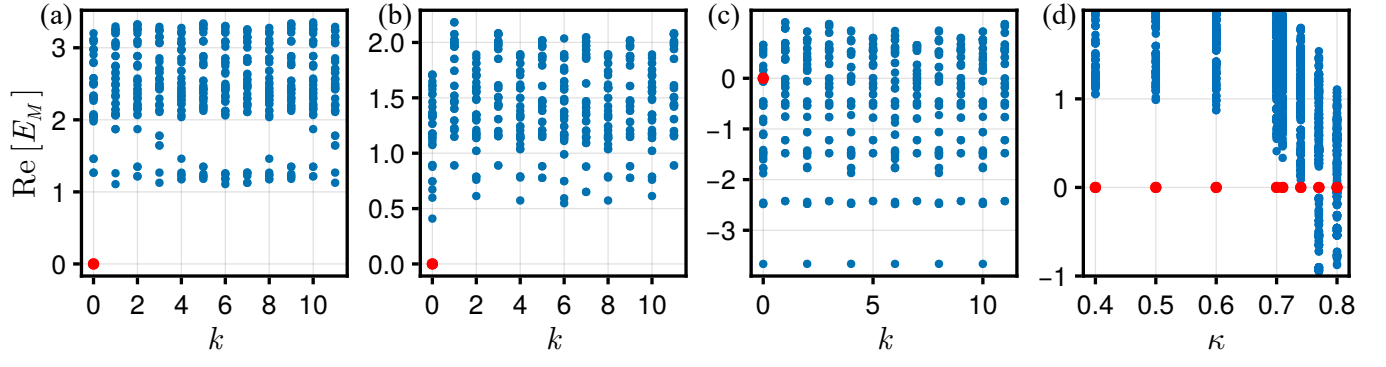


FIG. 13. Real part of the many-body energy spectrum for  $L_x = 6, L_y = 6, \phi = 1/3$ : (a)  $\kappa = 0$  (b)  $\kappa = 0.7$  (c)  $\kappa = 0.8$  (d) with respect to  $\kappa$ .